

# Reimagining the $e_g$ Electronic State in Oxygen Evolution Catalysis: Oxidation-State-Modulated Superlattices as a New Type of Heterostructure for Maximizing Catalysis

Ran Ding, Parisa Yasini, Haowei Peng, John P. Perdew, Eric Borguet,\* and Michael J. Zdilla\*

The discovery of solid-phase, inexpensive transition-metal-based water oxidation catalysts is a central goal for renewable energy, and has led to a general consensus that a partially populated metal  $e_g$   $d$ -electronic state is desirable, leading to favorable catalysis for certain elements in specific oxidation states. In manganese systems, the key species is manganese(III), whose high-spin  $d_4$  electronic configuration places an unpaired electron in the  $e_g$  orbital, which is postulated to contribute to electronic and structural features that support catalysis. Based on density functional theory calculations, it is predicted that electron transfer would be facilitated by a catalyst with alternating low- and high-Mn<sup>III</sup>-content sheets, which positions neighboring band edges in closer energetic proximity. The preparation of such catalysts is demonstrated for the first time and it is shown that the catalytic activity is maximized in these systems over more uniform, but more Mn<sup>III</sup>-rich systems. The best catalyst possesses alternating high- and low-average oxidation state sheets with interlayer Cs<sup>+</sup> ions, and has an overpotential of 450 mV at 10 mA, which represents an improvement of 250 mV over the best unmodified synthetic potassium birnessites. Using scanning tunneling spectroscopy, bandgap modulations consistent with the theoretically predicted band edge shifts are detected.

## 1. Introduction

Solar hydrogen remains the major target for renewable, alternative fuel because it is clean-burning, prepared from abundant water, and provides a potential means to fix and store solar energy.<sup>[1,2]</sup> The method of choice for hydrogen

production is water splitting due to the large abundance of water in the world. However, the water-splitting reaction has a thermodynamic standard potential of  $-1.23$  V, and is hindered by sluggish kinetics. Efforts to develop improved catalysts for both the proton reduction<sup>[2–4]</sup> and water oxidation half-reactions are a major focus of numerous research groups, though the latter oxygen evolution reaction (OER) is generally considered to be the greater challenge. OER is a particular challenge since large activation energies are typically associated with such catalysis, and release of reactive oxygen species (superoxide, hydrogen peroxide, hydroxyl radical) can damage catalysts.<sup>[5,6]</sup> Design of efficient electrocatalysts for electrochemical OER from water with low overpotential and long catalytic life is important to circumvent one of the largest barriers to a renewable hydrogen economy.

To the requirements of robust, inexpensive catalysts, transition metal oxides are of interest due to their stable structures and variable oxidation states.<sup>[7–12]</sup> A common advantageous property that has been repeatedly observed among a number of active transition-metal-containing water oxidation catalysts is an incompletely occupied  $e_g$  electronic state, that is, there should be an unequal population of the two higher-energy metal  $d$ -orbitals (Figure 1). The importance of the  $e_g$  state has been attributed to a number of factors, including the expected Jahn–Teller distortion, which has been argued to activate ligated oxygen atoms.<sup>[13,14]</sup> Electronic effects imparted by these species can create delocalized electronic states that facilitate electron transfer and hole migration.<sup>[13,15,16]</sup> For example, in first row transition metals, octahedral manganese(III),<sup>[13–20]</sup> intermediate-spin cobalt(III),<sup>[13,21]</sup> and nickel(III)<sup>[22]</sup>-based systems tend to show good activity, all of which possess an unequally populated  $e_g$  electronic state (Figure 1).

Among the various metal oxides, birnessite has been a subject of interest of our group<sup>[23–31]</sup> and those of others.<sup>[17,20,32–37]</sup> It is a layered manganese oxide material that consists of negatively charged Mn<sup>III/IV</sup>O<sub>2</sub> sheets with interstitial hydrated cations to balance the negative charge of the MnO<sub>2</sub> sheets (Figure 2). Past studies have led to a general consensus that

R. Ding, P. Yasini, J. P. Perdew, E. Borguet, M. J. Zdilla  
Department of Chemistry  
Temple University  
Philadelphia, PA 19112, USA  
E-mail: eborguet@temple.edu; mzdilla@temple.edu  
H. Peng, J. P. Perdew  
Department of Physics  
Temple University  
Philadelphia, PA 19112, USA



The ORCID identification number(s) for the author(s) of this article can be found under <https://doi.org/10.1002/aenm.202101636>.

DOI: 10.1002/aenm.202101636

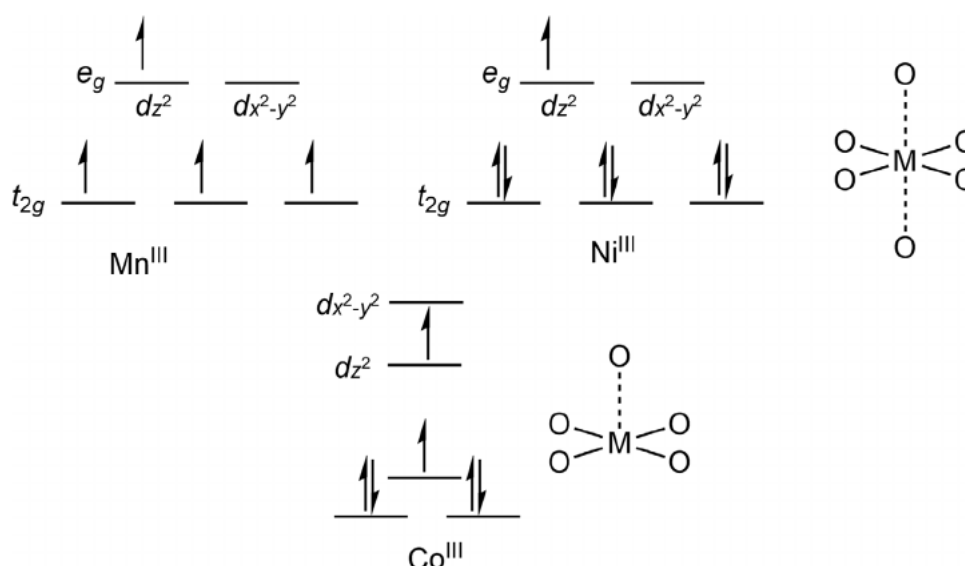


**Figure 1.** *d*-orbital splittings demonstrating the partial occupation of the  $e_g$  orbitals ( $d_{z^2}$ , but not  $d_{x^2-y^2}$ ) in  $\text{Mn}^{\text{III}}$ ,<sup>[13–20]</sup>  $\text{Co}^{\text{III}}$ ,<sup>[13,21]</sup> and  $\text{Ni}^{\text{III}}$ .<sup>[22]</sup>

there is a correlation between high catalytic activity and a high concentration of  $\text{Mn}^{\text{III}}$  in birnessite and other manganese oxides.<sup>[13–20]</sup> The larger ratio of  $\text{Mn}^{\text{III}}$  to  $\text{Mn}^{\text{IV}}$ , also referred to as a lower average oxidation state (AOS), leads to better catalytic performance.

Recent research from our group has focused on structure-performance relationships in birnessite, for which we have provided further evidence that enrichment of the birnessite sheets with increased  $\text{Mn}^{\text{III}}$  content,<sup>[24]</sup> or doping of sheets with cobalt<sup>[25,26]</sup> or copper<sup>[30]</sup> leads to improved activity. One prediction from our density functional theory (DFT) calculations, however, suggested that not only the abundance of  $\text{Mn}^{\text{III}}$ , but more importantly the distribution of  $\text{Mn}^{\text{III}}$  in birnessite, has a strong influence on the rate of electron transfer.<sup>[31]</sup> Kohn–Sham DFT solves self-consistent one-electron Schrodinger equations with a density-dependent effective potential that includes electron-electron interactions. These calculations predicted that a

“potential step” between a low-AOS ( $\text{Mn}^{\text{III}}$ -rich) and a high-AOS ( $\text{Mn}^{\text{IV}}$ -rich) sheet would place the conduction band of the high-AOS sheet closer in energy to both the valence band and a polaronic (localized  $e_g$   $\text{Mn}^{\text{III}}$ ) electronic state of the low AOS sheet (Figure 3). This energetic proximity between the empty states of one band and the filled states of the next is expected to facilitate electron transfer processes between the sheets and any interlayer species.

Earlier experiments to test this prediction relied on surface reduction of birnessite particles, which showed that as the AOS is lowered near the surface (but not in the bulk) the birnessite catalytic activity increases sharply, even in comparison to birnessite particles with low-AOS throughout.<sup>[31]</sup> However, birnessites with controlled layer-by-layer stacking of alternating layers of high- and low-AOS birnessite had not been prepared to offer a more direct experimental test of the computationally<sup>[31]</sup> investigated materials, nor had the DFT-predicted electronic structures that lead to this behavior been verified experimentally.

In this study, a previously reported exfoliation protocol<sup>[29,38]</sup> is used to prepare single-layer nanosheet suspensions of metal oxide samples for the assembly of few-layer electrocatalytically active samples with controllable stacking structures. Since interlayer cations have been shown to play an important role in the catalytic activity of birnessite, we further seek to clarify the structure-activity relationship relating to the interlayer region by constitution of the interlayer with an array of different Group 1A counteranions. We present here the marked effect of the non-uniform distribution of  $\text{Mn}^{\text{III}}$  on creating the theoretically predicted potential steps between low- and high-AOS layers, and the resulting enhancement of the OER catalytic activity of birnessite over homogeneously distributed  $\text{Mn}^{\text{III}}$ -rich samples. Further, we confirm the theoretically predicted collapse of the effective bandgap in two-layer samples using scanning tunneling spectroscopy (STS). The results provide a holistic view of this new role of  $\text{Mn}^{\text{III}}$  in OER catalysis, linking the theoretical and experimental electronic structure

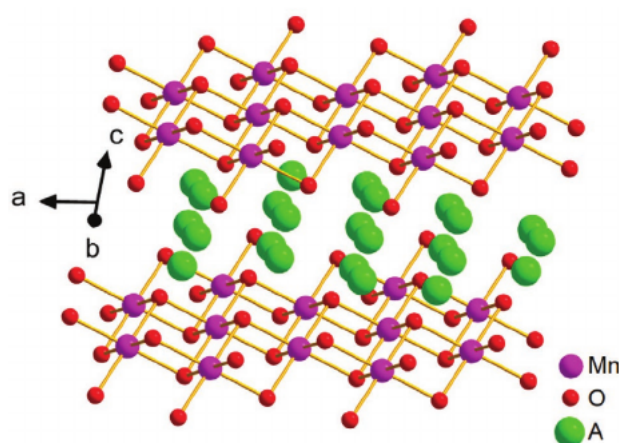


**Figure 2.** Crystal structure of birnessite (A = alkali metal cation). Water molecules are omitted for clarity.

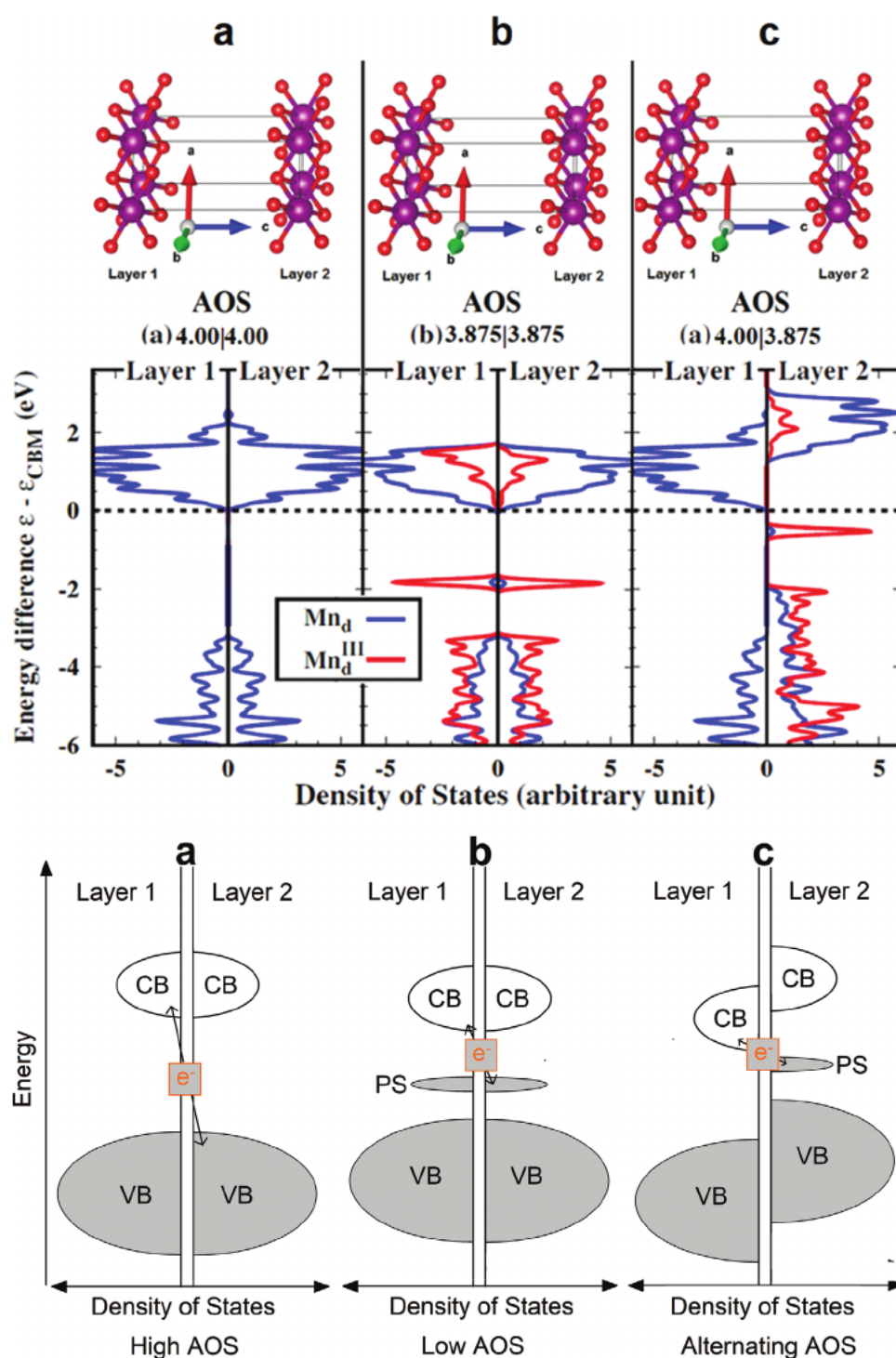


**Figure 3.** Top: periodic DFT-computed<sup>[31]</sup> DOS for a) high-AOS (4.00, all- $\text{Mn}^{\text{IV}}$ ) birnessite, b) lower-AOS (3.875) birnessite, and c) alternatively stacked high-low oxidation state birnessite. Bottom: Cartoon representation of band structure illustrating increasing facility of  $e^-$  transfer across sheets from left→right. VB = valence band; CB = conduction band; PS = polaron state (partially occupied  $e_g$  states).

to the catalytic activity of birnessite, and demonstrate that the judicious distribution of  $\text{Mn}^{\text{III}}$  in alternating layers gives superior catalysis to more  $\text{Mn}^{\text{III}}$ -rich systems. The results suggest that such alternating-sheet strategies could be a promising general approach for the design of new layered materials for redox catalysis.

## 2. Results

### 2.1. Few-Layer Birnessite Electrocatalysis for OER

Few-layer birnessite catalysts were prepared by controlled stacking of single layers using a previously reported

approach.<sup>[29]</sup> Two birnessite samples with different AOS were prepared. High-AOS birnessite (Birnessite A) was prepared by pyrolysis of potassium permanganate at a high temperature.<sup>[39]</sup> The low-AOS birnessite (Birnessite B) was prepared from Birnessite A by treatment with the two-electron reductant sodium dithionite. The AOS of Birnessites A and B are about  $\approx 3.85$  and  $\approx 3.70$  respectively, determined by a combination of inductively coupled plasma optical emission spectroscopy (ICP-OES) and redox back titration as described in the experimental section (Figure 4, Tables S1–S3, Supporting Information). Surface AOS was assessed using X-ray photoelectron spectroscopy (XPS, Figure S5, Supporting Information), which shows the expected lower Mn 3s splitting in the untreated birnessite sheets (A, 4.41 eV) in comparison to reduced birnessite sheets (B, 4.47 eV). Examination of the average oxidation by fitting<sup>[40]</sup> of the Mn 2p XPS (Figure S5, Supporting Information) of the samples gave AOSs of 3.77 and 3.67 for the regular (A) and reduced (B) birnessites, respectively, qualitatively similar to the AOS measured by back titration, but slightly more reduced. Since XPS is a surface technique, the result suggests the surface of birnessite is slightly more reduced than the bulk, a phenomenon which we have observed and reported previously.<sup>[31]</sup> Because this work involves the exfoliation of bulk birnessite and reassembly of the nanosheets, we consider the bulk ICP-OES/back titration measurement of AOS to be more representative of the reconstructed few-layer samples.

These samples were each exfoliated into single-layer nanosheets of manganese oxide by stirring in a solution of tetrabutylammonium hydroxide (TBAOH). The nanosheets are deposited onto a polyethylenimine-coated electrically conductive fluorine-doped tin oxide (FTO) surface as an electrochemically active substrate. The assembly approach<sup>[29]</sup> permits controlled layer-by-layer deposition by repeated dipping into nanosuspension, followed by a solution of the cation source, followed by the nanosuspension again (etc.) to reassemble few-layer birnessites with controlled layer-by-layer composition.

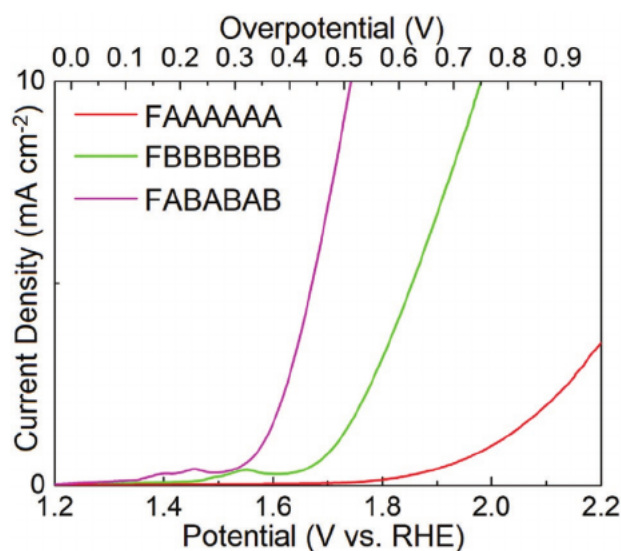


**Figure 4.** LSV polarization curves of few-layer birnessite composed of A) six high AOS birnessite sheets, B) six low AOS sheets, and six layers of alternating A/B sheets. “F” Designates the FTO electrode substrate.

We initially examined six-layer samples of high-AOS birnessite (A) and low-AOS birnessite (B), each deposited onto the FTO substrate, that is: FAAAAAA and FBBBBBB, where F = FTO. Each sample was reconstituted with  $K^+$  counteranions in between layers. This assembly permits examination of electrocatalytic activity of the few-layered catalysts using linear sweep voltammetry (LSV), where the sample is immersed into an aqueous solution, and the electrode potential of the FTO is swept toward positive values. The onset of redox activity results in a positive measured current, and an exponentially rising curve indicates catalysis due to redox-induced current through the circuit. Catalytic activities are compared by measuring the overpotential ( $\eta$ , the potential beyond the thermodynamic water oxidation potential of 1.23 V vs the reversible hydrogen electrode (RHE)) required to reach a current of 10 mA, and by the Tafel slope ( $b$ , voltage change required for a tenfold current increase). Both of these parameters are related to how much extra energy is required to drive the catalytic reaction over the activation barrier, and thus the best catalysts have low values of  $\eta$  and  $b$ .

As shown in the LSV polarization curves (Figure 4), sample FAAAAAA shows an overpotential that is larger than 1000 mV at a current density of  $10 \text{ mA cm}^{-2}$ , and a large Tafel slope of  $340 \text{ mV dec}^{-1}$  (Figure S6, Supporting Information), which is expected due to the low  $Mn^{III}$  content. Reduced birnessite FBBBBBB shows several small redox features at about 1.4–1.5V versus RHE that we attribute to the reduction of defect Mn sites in birnessite. These features are followed by the catalytic wave at a significantly reduced  $\eta$  of 750 mV, and a reduced  $b$  of  $180 \text{ mV dec}^{-1}$  (Figure S6, Supporting Information), confirming well-established knowledge that low-oxidation-state, manganese(III)-rich systems favor OER catalysis. This phenomenon is attributed to the different electron configurations of the manganese in  $Mn^{IV}$  versus  $Mn^{III}$ . In the former, the metal-based 3d electrons of the metal are in the configuration  $t_{2g}^3 e_g^0$ . Reduced birnessite contains more  $Mn^{III}$  with the electron configuration  $t_{2g}^3 e_g^1$ .

We next examined an alternatively stacked sample: FABABAB for comparison to the electronically uniform compositions (Figure 4). Despite the mixed material having lower overall  $Mn^{III}$  content than sample FBBBBBB, these catalysts exhibit a significantly smaller overpotential of  $\approx 510 \text{ mV}$  (Figure 4) and an improved Tafel slope of  $105 \text{ mV dec}^{-1}$  (Figure S6, Supporting Information). The improved OER catalytic activity indicates that the catalysis is enhanced not only by the abundance of  $Mn^{III}$  states, but also by the alternating spatial distribution of  $Mn^{III}$  in the stacking direction.

To investigate how the location of potential steps (A-B junctions, shown in boldface) affects OER catalysis, we have prepared few-layer birnessites with additional variations in the order and composition of A and B sheets. In particular, these experiments were designed to test several competing hypotheses for the most effective catalytic structure. These competing hypotheses are: 1) That a larger number of A-B junctions should give the greatest catalysis. 2) Having an AB junction near the electrode (to minimize hole migration distance) is advantageous, 3) that having the AB potential step near the solvent surface is advantageous in order to access the substrate, and 4) that a larger and more abrupt potential step in the center of



the stack (e.g., AABBB) might be advantageous over a more averaged structure with more potential steps (e.g., ABAB). In these experiments, all few-layer birnessite samples are prepared by stacking 8 layers of manganese oxide sheets with interleaving potassium counteranions.

In the first set of experiments, we stack 7 layers of one type and one layer of the other type, and examine the effect of having the potential step near the electrode surface versus near the solvent interface. Thus, four compositions are tested: FABBBBBBB, FBBBBBBBA, FBAAAAAAA, FAAAAAAB. From the polarization curve (Figure 5A), we find that the relative catalytic activity of these birnessites, from best to worst, is FABBBBBBB, FBBBBBBBA, FBAAAAAAA, and FAAAAAAB. The results suggest that birnessites with a predominantly low AOS (B-rich) composition are generally better than those which are predominantly composed of A, no matter where the “AB” potential step is. However, the insertion of at least one A layer

improves catalysis over a purely B-containing sample. Second, the samples with the AB potential step nearer the electrode are superior to the samples with the AB potential step near the solvent, suggesting that the electron transfer facilitated by the AB potential step near the electrode is a more important feature than solvent/substrate access near the AB potential step. The overpotential for water oxidation catalysis by the best sample, FABBBBBBB (Figure 5A, magenta) is 480 mV and has a Tafel slope of 102 mV dec<sup>-1</sup> (Figure S7, Supporting Information), slightly better but similar to the six-layer FABABAB sample shown in Figure 4.

The long-term performance was investigated using chronoamperometry (Figure S10, Supporting Information). FAAAAAA, FBBBBBB, and FABABAB were held at constant potential. FAAAAAA was held at 2.0 V versus RHE ( $\eta = 0.7$  V) and exhibits the lowest current and stability, dropping from 2.8 mA cm<sup>-2</sup> to  $\approx 1.6$  mA cm<sup>-2</sup> over 10 min, and then exhibits a slow, gradual decline in activity over the next hour. FBBBBBB, despite being held at a lower potential of 1.85 V versus RHE ( $\eta = 0.55$  V) shows better activity than FAAAAAA. After a rapid drop in current from 4.1 to 2.2 mA cm<sup>-2</sup> at the start of the measurement, the current then gradually rises to 2.6 mA cm<sup>-2</sup> over the course of an hour. Its activity never drops below that of FAAAAAA. FABABAB, held at the lowest potential of 1.7 V versus RHE ( $\eta = 0.4$  V) shows the best performance, with the current dropping from 5.5 mA cm<sup>-2</sup> much more gradually to 2.9 mA cm<sup>-2</sup> over the course of an hour. Its activity does not drop below that of the other two samples during this time. Chronoamperometry thus confirms that the general trend (activity of AA < BB < AB) holds over time, and not just at the start of catalysis.

It is also noteworthy from Figures 4 and 5a that the overpotentials of sample FABBBBBBB and sample FABABAB are very similar ( $\eta \approx 0.5$  V) as are their Tafel slopes (105 and 102 mV dec<sup>-1</sup> respectively, Figures S6 and S7, Supporting Information), which suggests that these two catalysts had similar activities, and that a potential step near the electrode is a more important consideration than the AOS of the distal layers. However, the sample FBAAAAAAA also has a potential step near the electrode, but exhibits lower catalytic performance ( $\eta = 0.65$  V, Tafel slope = 270 mV dec<sup>-1</sup>) illustrating that the composition of the distal sheets is also important, and that an ideal catalyst has a potential step near the surface, and must include additional B sheets in more distal layers to maximize activity.

In the next set of experiments, birnessite samples are composed of half A and half of B sheets (Figure 5B). The “AB” potential step(s) are located either in the middle of the structure via segregation of the A and B sheets, or throughout the structure by alternating the A and B sheets. In the first group, FAAAAAB and FBBBBAA, very similar overpotentials of 550 mV at a current of 10 mA cm<sup>-2</sup> (Figure 5B), and Tafel slopes of 175–180 mV dec<sup>-1</sup> (Figure S8, Supporting Information) are observed. In the second group, “FABABAB” and “FBABABA”, a lower overpotential around 510 mV is observed for both. Both samples have lower Tafel slopes than the segregated samples, though the FABABAB sample is lower (105 mV dec<sup>-1</sup>) than the FBABABA sample (150 mV dec<sup>-1</sup>). In this case, the catalytic activity is enhanced by the presence of multiple potential steps rather than a single potential step in the center of the stack, and

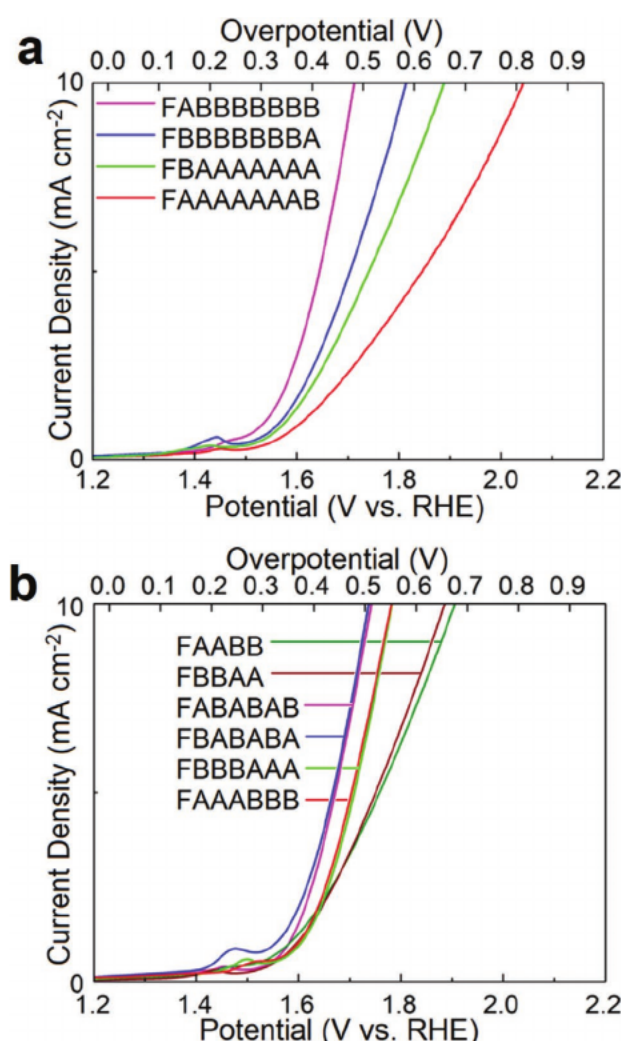


**Figure 5.** LSV polarization curves of few-layer birnessite sheets assessing a) The impact of the location of the potential step, close to or distal from the FTO electrode, on layered materials containing seven layers of one type and one layer of the other type. b) The influence of the first layer identity, A or B, on layered materials containing an equal number of A and B layers with layer types segregated or alternating.

catalysis is less affected by which layer (A or B) is next to the electrode. The result suggests that the ideal scenario involves the creation of numerous potential steps throughout the structure, likely facilitating hole transfer throughout the catalyst.

In a final set of experiments, four-layer FAABB and FBBA, were examined. The measured overpotentials are 670 and 650 mV, similar to each other, but higher than the six-layer analogs (Figure 5b). This demonstrates that while A-B potential steps are advantageous to catalysis, so also is the total number of layers, with more layers giving lower overpotentials. These observations are consistent with the most active catalytic layer being the potential step proximal to the electrode (Figure 5a) and suggest that distal layers provide some electronic enhancement effect that increases with increasing layer number.

Inspired by the work of Kurz,<sup>[32]</sup> Sawangphruk,<sup>[37]</sup> and Mendoza-Cortez,<sup>[20]</sup> which argued that cation identity has a strong effect on catalytic activity, we sought to investigate the effect of intercalated cations in reassembled structures, using the more effective alternating AB structures. Six-layer alternating (AB) samples of birnessite catalyst were prepared using Li<sup>+</sup>, Na<sup>+</sup>, K<sup>+</sup>, and Cs<sup>+</sup> as intercalated cations using the same substrate dipping protocol.<sup>[29]</sup> The result is illustrated in Figure 6. With the size of intercalated cations increasing from Li<sup>+</sup> to Cs<sup>+</sup>, the overpotential at a current of 10 mA cm<sup>-2</sup> declines from 640 mV for Li<sup>+</sup>, to 545 mV for Na<sup>+</sup>, 510 mV for K<sup>+</sup>, and 450 mV for Cs<sup>+</sup>, indicating a favorable effect for increased cation radius. Tafel slopes also gradually decrease, having values of 230, 130, 105, and 92 mV dec<sup>-1</sup> respectively (Figure S9, Supporting Information). This effect may be attributable to the decreased Lewis acidity of Cs<sup>+</sup>, which decreases the affinity of the cation for interstitial water. Past work from our group has shown that increased dynamical motion of water in the interlayer facilitates electron transfer; this effect may be enhanced by the expected weak binding between Cs<sup>+</sup> and H<sub>2</sub>O.<sup>[23]</sup> It is curious to note that this trend is opposite of that observed by Kosasang et al.,<sup>[37]</sup> and may reflect a difference in the chemical synthesis of these

materials by Kosasang et al. versus the layer-by-layer assembly used here.

## 2.2. Scanning Tunneling Spectroscopy

While the results of catalysis are consistent with the hypothesis derived from DFT that proximity between the filled states of B and the empty states of A would facilitate electron transfer, the catalysis results are not a direct confirmation of the predicted density of states (DOS). To examine the predicted effect on band structure we turned to STS, which uses the tip of a Scanning Tunneling Microscope (STM) in order to measure the tunneling current as a function of the bias between the STM tip and the substrate at a constant tip-sample separation. The increase of current towards negative values at negative bias voltages corresponds to the removal of electrons from the valence band, while the increased current at positive bias voltages corresponds to the addition of electrons to the conduction band. The differential conductance ( $dI/dV$ ) is used to measure the surface DOS.

STM samples were prepared as follows. To avoid the insulating effect of organic chemicals, PEI and TBOH were avoided. Birnessite samples, A and B, were therefore exfoliated using a chemical-free sonication approach.<sup>[41,42]</sup> Samples were drop cast in two steps onto conducting gold-on-mica (G) substrates: First a layer of nanosheets (A or B) was drop cast and air-dried, followed by a layer of K<sup>+</sup> ions, followed by a second layer of nanosheets (A or B), a second layer of K<sup>+</sup> ions for charge neutrality, and finally, a water rinse to remove excess salt. Each drop-cast step was designed using an idealized concentration for the deposition of a monolayer (of A or B) on average. STM images were taken to identify multiple atomically flat regions, and to position the STM tip on the center of sheets, far away from edges and possible defects (see Figure S11, Supporting Information). The I-V curves were collected in two to six separate locations on each substrate (to check for consistency across the sample). Typically, 10 potential sweeps were recorded and averaged for each location so that the I-V curves presented in Figure 7 are the average of a total of ~20–60 curves. While an unmodified gold substrate (G) shows metallic behavior, birnessite bilayers on gold show semiconductor-like characteristics with measurable bandgaps. As predicted, the high oxidation state birnessite (GAA) has the largest bandgap (2.5 eV, Figure 7, red), while reduced birnessite (GBB) has a lower bandgap of 0.7 eV. The mixed sheet materials (GAB, GBA), despite containing a layer of A, show no remnant of the large bandgap of GAA, and instead show bandgap values smaller than the reduced birnessite bilayer (GBB). Sample GBA (Figure 7, blue) shows a bandgap of 0.4–0.5 eV based on the derivative plot of the STS data (Figure S12, Supporting Information, with a threshold differential current cutoff of 5 nA V<sup>-1</sup>), and with a similar conduction band minimum (CBM) but with a raised valence band maximum (VBM). The opposite-ordered stack, sample GAB (Figure 7 violet) also shows a reduced bandgap even more visually pronounced, though the  $dI/dV$  plot (Figure S12, Supporting Information) also measures the bandgap at ~0.4 eV. In contrast to GBA, the conduction VBM is relatively unchanged, while lowering of the CBM is apparent (Figure 7, bottom).

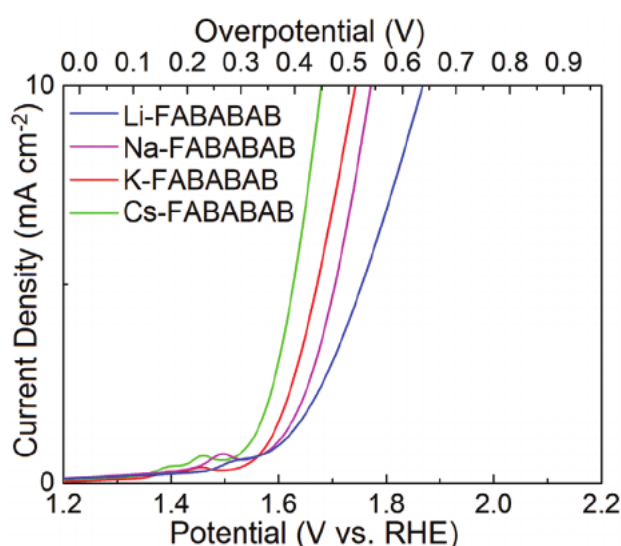


**Figure 6.** LSV polarization curves of six-layer birnessite samples composed of alternating A/B sheets with different intercalated cations.

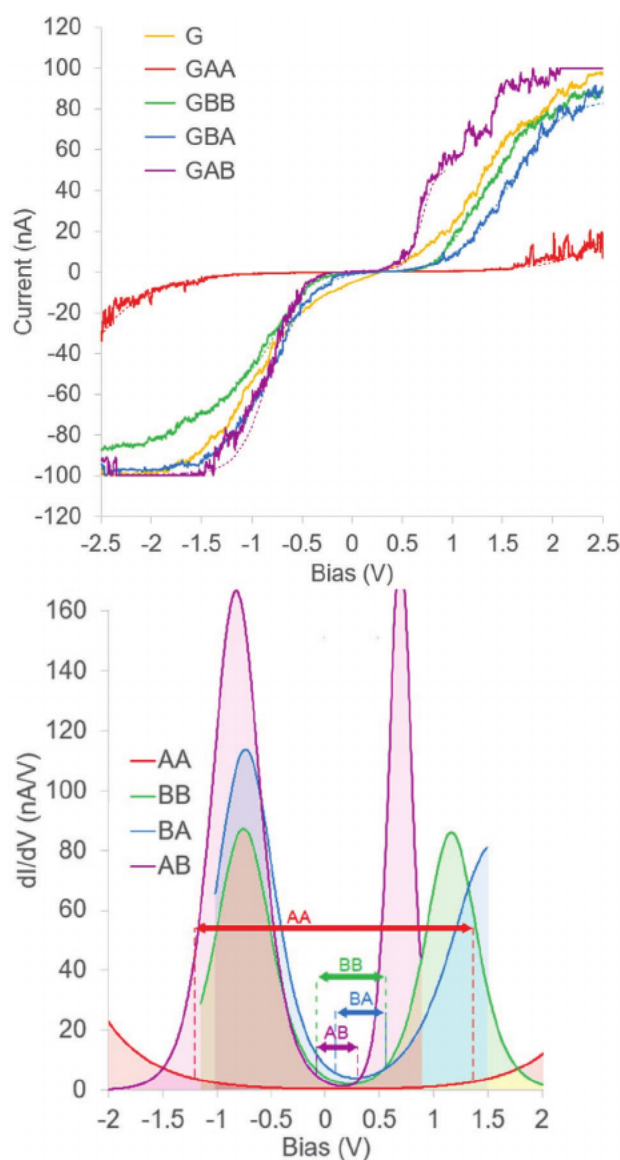


**Figure 7.** Top: STS on  $\text{MnO}_2$  nanosheet bilayers with sigmoidal fits shown as dotted lines. Bottom: integral of the STS fits with area under curves shaded, giving an experimental density of states. Band edges are illustrated with dotted lines, and band gaps are shown as double arrows. Fit equations and parameters, and band edge positions determined from experimental plots of  $dI/dV$  are given in the Supporting Information.

### 3. Discussion

There has long been a consensus that  $\text{Mn}^{\text{III}}$  is important for catalysis in manganese oxide minerals. Efforts to deconstruct experimental observations and uncover the underlying physical basis for this phenomenon have led to a number of explanations. The major theme that arises is that the Jahn–Teller distortion that results from an unequal population of the  $e_g$  electronic state is key to catalytic activity.<sup>[13–20]</sup> While there is a general consensus about the importance of this electronic feature, a number of orthogonal explanations for its role have emerged. These include arguments from Rao and Dismukes that an unequally populated  $e_g$  results in a high binding affinity

for  $\text{O}_2$  and the corresponding weakening of the  $\text{O}=\text{O}$  double bond by interaction with the electron occupying an Mn-based  $e_g$  orbital.<sup>[13,14]</sup> Other work from Dismukes has argued that a trigonal Jahn–Teller distortion of the Mn geometry (as opposed to the more commonly invoked tetragonal distortion, i.e., axial lengthening) results in a more robust Mn–O bonding framework, improving catalysis.<sup>[17]</sup> This group also argued that the weakening of Mn–O bonds by  $e_g$  occupation improves atomic flexibility, facilitating turnover.<sup>[14,15]</sup> The group of Nocera argued that in their systems, a lower-coordinate  $\text{Mn}^{\text{III}}$  induces lattice strain that reduces the bandgap.<sup>[15]</sup> A number of reports, such as one from Rao<sup>[13]</sup> invoke that the presence of the high-energy  $e_g$  electron facilitates rapid electron transfer. Navrotsky and coworkers argued that the most active catalysts they examined (calcium-containing manganese oxides) exhibited a variable ratio of  $\text{Mn}^{\text{III}}$  and  $\text{Mn}^{\text{IV}}$ , suggesting a plateau of stability across a wide range of  $\text{Mn}^{\text{III}}/\text{Mn}^{\text{IV}}$  ratios, which implied  $\text{Mn}^{\text{III}}$  and  $\text{Mn}^{\text{IV}}$  states are in equilibrium in these catalysts. A related argument from Mendoza-Cortes and coworkers suggested that distorted  $\text{Mn}^{\text{III}}$  sites are stabilized by neighboring  $\text{Mn}^{\text{IV}}$  atoms, which can help compensate for the buildup of negative charge, but that closely spaced (neighboring)  $\text{Mn}^{\text{III}}$  are unstable, and promote catalysis.<sup>[20]</sup> In this same work, the authors argued that hard cations (i.e., charge dense) stabilize the  $\text{Mn}^{\text{III}}$  sites by coordinating to the negatively charged Jahn–Teller distorted oxygen atom.

While numerous advantages of  $\text{Mn}^{\text{III}}$  are probably synergistic, the suggestion that non-uniform (periodic or not) atomic distributions of  $\text{Mn}^{\text{III}}$  across different sheets are advantageous is a rather newer argument,<sup>[31]</sup> and has not been conclusively demonstrated in catalysts judiciously assembled layer-by-layer in a controlled fashion before this work. Since previous conclusions all supported catalytic enhancement by a large amount of  $\text{Mn}^{\text{III}}$ , (or at least an even mixture of  $\text{Mn}^{\text{III}}$  and  $\text{Mn}^{\text{IV}}$ ),<sup>[16,20]</sup> the most reduced birnessites (BB) would probably be the best catalysts, and the alternatively stacked birnessites (AB) would be better than the high-AOS birnessites (AA), but perhaps not quite as good as the low AOS (BB) birnessites. By contrast, according to our theoretical hypothesis, the alternatively stacked birnessites could match or even exceed the low AOS (BB) samples. We tested this hypothesis by comparing the activity of AB-type samples to the BB-type samples. We further experimentally searched for the optimal atomic and device configuration, which was unfeasible for atomic simulations. We indeed found a good catalytic activity from several configurations with a non-uniform  $\text{Mn}^{\text{III}}$  distribution. In particular, the AB-type catalysts surprisingly far outperformed both the high- and low-AOS samples, despite having less  $\text{Mn}^{\text{III}}$  overall than the low-AOS samples; from the ICP-OES back-titration experiments, the BB-type samples (3.70) have a lower AOS than the expected value for AB-type birnessites of 3.775 (this value is presumed to be the average of the BB- and AA-type birnessite AOS values: 3.70 and 3.85 respectively). Given that birnessite is normally among the poorer OER catalysts (normally with an overpotential of at least 0.7 V at 10 mA current), the achievement of such low overpotential (0.45 V for the best sample), is a remarkable reduction of overpotential by 250 mV without a fundamental change in composition.

While the catalytic result is consistent with the hypothesis that alternating AB birnessites would facilitate layer crossing



by electrons and holes, an experimental validation of the calculated density of states using STS adds confidence to the interpretation. We examined drop-cast bilayers of birnessites using STS. Using equivalent concentrations for all nanosuspensions, we assembled bilayer samples of high-AOS (A) and low-AOS (B) birnessite sheets on gold-on-mica substrates (G). Sample GAA showed a very large bandgap of 2.5 eV, while the more reduced sample GBB showed a reduced bandgap of 0.7 eV. Samples GBA and GAB both showed a bandgap lowering to  $\approx 0.4$  eV, even lower than sample GBB, however with different edge positions. In Sample GBA, the VBM was raised, while in GAB, the CBM was lowered. This is consistent with the hypothesis that the energetic proximity of the CBM and the VBM (or the top of the polaronic state) puts the layers in improved electronic communication, and that electrons can tunnel between the polaronic state of one layer and the conduction band of the other. The explanation is illustrated in **Figure 8**. In panel 1, a wide bandgap results from a DOS with a smaller polaronic state due to a lower concentration of  $\text{Mn}^{\text{III}}$ . In panel 2, a more significant small polaron state resulting from more  $\text{Mn}^{\text{III}}$  gives a lower observed bandgap. In Panel 3, a B layer is stacked next to an A layer, with the STM tip against the higher-AOS A layer. In the mixed A-B samples, some electron transfer between the layers results in a more  $\text{Mn}^{\text{III}}$ -like A-layer than in panel 1 due to interelectronic communication. In panel 3, the CBM appears at a similar energy to GBB, though the apparent VBM is raised due to cross-layer communication with the higher-energy VBM of B. In Panel 4, the VBM appears at a similar energy to GBB, though the apparent CBM is lowered due to cross-layer communication with the lower-energy CBM of A. While these images are qualitative in nature, they illustrate the consistency of the hypothesis that alternating AB layers improve electronic

communication across layers, promoting catalysis, and explain the change in band edge energies observed by STS.

## 4. Conclusions

While there has long been a general consensus that  $\text{Mn}^{\text{III}}$  content is advantageous in manganese-based OER catalysts, this work demonstrates conclusively for the first time that distribution of  $\text{Mn}^{\text{III}}$  in the stacking direction is more important for catalysis in birnessite than overall  $\text{Mn}^{\text{III}}$  content. Despite a lower overall  $\text{Mn}^{\text{III}}$  content, alternating AB stacks showed improved catalytic activity over more  $\text{Mn}^{\text{III}}$ -rich all-B stacks. Supporting this observation, STS showed lower measured band gaps in the alternatively stacked sheets consistent with improved electronic communication across the  $\text{MnO}_2$  layers. In examining the different arrangements of A-B stacks, we found that samples with potential steps near the electrode showed better performance than those with potential steps more distal from the electrode. Furthermore, in general, numerous potential steps (ABAB) showed superior catalytic activity over samples with only one step (BAAA or ABBB), though low-AOS (B-rich) samples with a potential step near the surface also had high activity (e.g., ABBB). The presence of potential steps showed improved activity over  $\text{Mn}^{\text{III}}$ -rich (BBBB) samples in all cases. The identity of interlayer cations also plays an important role, with larger alkali cations ( $\text{Cs}^+$ ) showing superior performance over smaller ones ( $\text{Li}^+$ ). This may be due to the role of harder cations in stabilizing the small polaronic states associated with Jahn–Teller distorted  $\text{Mn}^{\text{III}}$ , which was predicted from theory.<sup>[20]</sup> Future reports will unveil our work demonstrating that this is a general phenomenon by reporting related observations in layered cobalt and nickel mono- and bimetallic systems for OER. Experiments

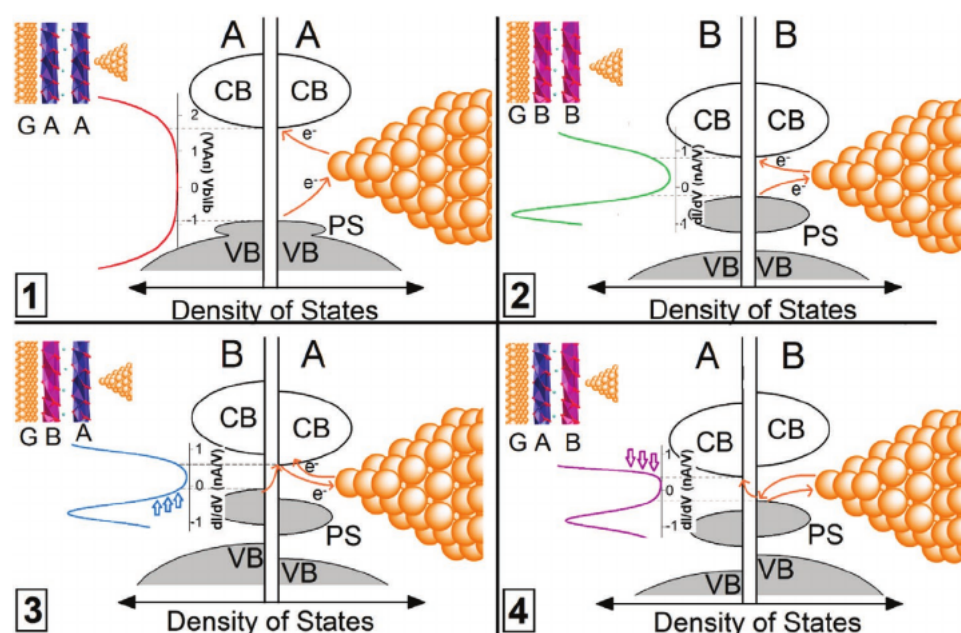


**Figure 8.** Cartoon description of STS experiment on birnessite bilayers on gold. In the upper left corner of each panel, a diagram of the bilayer is illustrated. A simplified representation of the DOS is shown in the center of each panel, aligned with the experimental STS ( $dI/dV$ ) to the left. At the right of each panel, arrows show the motion of electrons between the STM tip and the band edges. Cross-layer communication raises the effective VBM in panel 3 (blue arrows) while it lowers the effective CBM in panel 4 (purple arrows).



to explore the possibility of the influence of potential steps on other types of redox catalysis, such as the hydrogen evolution reaction, or one-carbon redox chemistry are also underway.

## 5. Experimental Section

**General:** X-ray powder patterns were obtained on a Bruker D8 Discovery powder X-ray diffractometer and Cu K $\alpha$  radiation from a sealed tube with a graphite monochromator. XPS of the dry samples were collected with a Thermo Scientific K-alpha+ at the University of Delaware. TEM samples were prepared by depositing one drop of sonicated sample in water (100 mg L<sup>-1</sup>) on a lacey carbon copper mesh TEM grid (400 mesh, Ted Pella) and allowed to air dry. Images were collected using a JEOL JEM-1400 microscope operating at 120 kV. Elemental analysis was performed using a Thermo Scientific iCAP 7000 Series ICP-OES.

**Synthesis of Potassium Birnessite:** Birnessite with high AOS was prepared by calcination of finely grained KMnO<sub>4</sub> powder at 600 °C for 5 h. This approach<sup>[39]</sup> gives high-AOS triclinic birnessite which was less active than the low-AOS hexagonal birnessite prepared by solution methods.<sup>[43]</sup> However, this solid-state approach gives better reproducibility for controlled experiments on slightly-varied AOS samples. The reliably poor activity of the high-AOS starting materials helped in the positive identification of conditions that favor the enhancement of catalytic activity. At the end of the calcination, all products were washed with water, filtrated and dried repeatedly until PXRD showed no byproduct was detected. Reduced birnessite with low AOS was made by adding original birnessite into a solution of sodium dithionite with the equivalent ratio of 4:1 (Mn : Na<sub>2</sub>S<sub>2</sub>O<sub>4</sub>) and then stirring overnight.

**X-Ray Photoelectron Spectroscopy:** XPS of the dry samples were collected using monochromatic Al K $\alpha$  X-rays (148.7 eV) generated from a rotating anode with a high resolution, 300 mm mean radius hemispherical electrostatic analyzer. The base pressure of the analysis chamber was maintained at 1 $\times$ 10<sup>-9</sup> Torr. Survey scans were collected using fixed pass energy of 300 eV and narrow scans were collected using a fixed pass energy of 150 eV. Data collected for the Mn 2p spectral region was peak fitted using Casa XPS software.

To fit the Mn 2p<sub>3/2</sub> region, the procedure used by Nesbitt was employed that considers the multiplet structure resulting from the presence of unpaired valence electrons in the 3d orbitals of manganese in the birnessite.<sup>[44]</sup> This fitting procedure relies on the theoretical calculations by Gupta<sup>[45]</sup> of the expected XPS spectra from the free Mn(IV), Mn(III), and Mn(II) ions. The prior work showed that the calculated XPS spectra for the free ions containing 5 multiplet peaks allowed the accurate fitting of experimental XPS Mn 2p<sub>3/2</sub> data for birnessite. The contributions of the Mn(IV) to the XPS data were fitted with peaks at 642.15, 643.19, 644.0, 645.05, and 646.06 eV using a relative peak area ratio of 1:0.63:0.32:0.10:0.06. Mn(III) contributions to the XPS data were fitted with peaks at 640.83, 641.53, 642.34, 643.36, and 644.73 eV with a relative peak area ratio of 1.0:0.71:0.42:0.30:0.30. Peak area ratios for each Mn-species were not changed during the fitting procedure. Peaks with a 50:50 Gaussian:Lorentzian contribution were used in the procedure and the full width half maximum (FWHM) for each peak was 1.15 eV. Using these parameters the spectral data was fitted by varying the relative contribution of individual sets of multiplet peaks.

**Determination of Mn Content:** To determine total Mn content, 0.50g of birnessite was dissolved in hydroxylamine hydrochloride (0.25M, 20mL) and diluted to 250mL. Mn content was then determined by analysis of an aliquot of the diluted solution by ICP-OES.

**Oxalic-Permanganate Back Titration to Determine the Oxidation State of Mn:** 0.2 g of the birnessite sample was dissolved in 5 mL solution of 0.5 mol L<sup>-1</sup> oxalic acid and 10 mL solution of 1 mol L<sup>-1</sup> H<sub>2</sub>SO<sub>4</sub> to reduce the birnessite to Mn<sup>2+</sup> solution. The excess oxalic acid was back-titrated with standardized KMnO<sub>4</sub> solution at 75–85 °C to obtain the oxidation number of Mn. AOS was calculated according to both the titration result and the total Mn amount.<sup>[46]</sup>

**Synthesis of MnO<sub>2</sub> Nanosheets:** The intercalated K<sup>+</sup> was removed by acid exchange by stirring 0.2g materials in diluted HNO<sub>3</sub> solution

(0.1 M, 10mL) for 2 days. The suspension was centrifuged at 7000 rpm and washed with water until pH was 6–7. Then the proton-exchange material suspension was added to an aqueous solution of TBAOH to perform exfoliation. After stirring for 10 days, the TBAOH solution was removed by centrifugation at 14 000 rpm for 15 min and the precipitate was collected and washed with water and ethanol and subsequently redispersed into water to form a colloidal solution of purified NS. Finally, the exfoliated NS supernatant was isolated from the colloidal solution by centrifugation at 7000 rpm for 15 min.

**Assembly of MnO<sub>2</sub> Nanosheets into Few Layer Materials:** This layer-by-layer assembly procedure was based upon the descriptions used in previous studies.<sup>[29]</sup> First, an 1cm $\times$ 1cm sample of FTO was washed with acetone, ethanol, and water, and dried in air. The substrate, dry FTO, then was immersed in to a Polyethylenimine (PEI) solution (2.5g L<sup>-1</sup>) for 1 min to be coated. After rinsing with water 3 times and drying in air, the PEI-precoated FTO was dipped into the colloidal solution of Mn-NS for 1 min to form an ultra-thin NS layer. After that, the film was immersed into a KCl solution (5 mM) for 1 min, then rinsed with water and dried. Afterwards, the film with absorbed K<sup>+</sup> returned into a NS solution to form a bilayer NS with interlayer K<sup>+</sup>. Repeatedly immersing it into NS and KCl solution was carried out to assemble (NS/K<sup>+</sup>)<sub>n</sub> layered materials. The process is illustrated in Figure S1, Supporting Information.

**Electrochemical Measurements:** Electrochemical characterization of the various layered materials was performed in 1 M KOH using a CH Instrument electrochemical analyzer (model CHI660E), a Pt wire counter electrode, a saturated calomel electrode (SCE), and an FTO (1 cm $\times$ 1 cm) working electrode (coated with the layered material of interest). The measured potentials versus SCE were converted to the RHE scale via the Nernst equation

$$E_{\text{RHE}} = E_{\text{SCE}} + 0.059\text{pH} + E_{\text{SCE}}^{\circ} \quad (1)$$

where  $E_{\text{RHE}}$  is the converted potential versus RHE,  $E_{\text{SCE}}$  is the experimental potential measured against SCE reference electrode, and  $E_{\text{SCE}}^{\circ} = 0.2412\text{V}$  at 25°C. The electrocatalysis was measured using LSV with a scan rate of 10 mV s<sup>-1</sup>.

**STS/STM:** STM imaging and STS measurements were performed using an Agilent 4500 (Molecular Imaging) microscope under ambient conditions using a mechanically cut Pt-Ir (9:1) wire (diameter 0.25 mm) as an STM tip, purchased from Alfa Aesar. All samples were prepared by drop-casting the materials on Au(111) on mica purchased from Phasis Sàrl, Geneva-Switzerland. Prior to the deposition step, the Au(111) on mica was H<sub>2</sub>-flame annealed and cooled down in the air. All the STM imaging was performed in constant current mode. Gwyddion software was used for the visualization of STM images. All STS data (I-V curves) were analyzed and fitted using Igor Pro software.

## Supporting Information

Supporting Information is available from the Wiley Online Library or from the author.

## Acknowledgements

This work was supported as part of the Center for Complex Materials, an Energy Frontier Research Center funded by the US Department of Energy (DOE), Office of Science, Basic Energy Sciences under Award DE-SC0012575.

## Conflict of Interest

The authors declare no conflict of interest.

## Data Availability Statement

The data that support the findings of this study are available from the corresponding author upon reasonable request.

## Keywords

catalysis, electrochemistry, layered materials, manganese oxides, oxygen evolution reaction, scanning tunneling spectroscopy, water oxidation

Received: May 26, 2021

Revised: August 31, 2021

Published online: October 1, 2021

- [1] N. S. Lewis, G. Crabtree, A. J. Nozik, M. R. Wasielewski, P. Alivisatos, H. Kung, J. Tsao, E. Chandler, W. Walukiewicz, M. Spitler, R. Ellingson, R. Overend, J. Mazer, M. Gress, J. Horwitz, C. Ashton, B. Herndon, L. Shapard, R. M. Nault, *Report of the Basic Energy Sciences Workshop on Solar Energy Utilization*, DOE SC (USDOE Office of Science (SC)), United States **2005**.
- [2] M. G. Walter, E. L. Warren, J. R. McKone, S. W. Boettcher, Q. Mi, E. A. Santori, N. S. Lewis, *Chem. Rev.* **2010**, *110*, 6446.
- [3] H. Wang, L. Gao, *Curr. Opin. Electrochem.* **2018**, *7*, 7.
- [4] X. Chia, A. Y. S. Eng, A. Ambrosi, S. M. Tan, M. Pumera, *Chem. Rev.* **2015**, *115*, 11941.
- [5] M. W. Kanan, D. G. Nocera, *Science* **2008**, *321*, 1072.
- [6] M. Gong, H. Dai, *Nano Res.* **2015**, *8*, 23.
- [7] Z.-L. Wang, D. Xu, J.-J. Xu, X.-B. Zhang, *Chem. Soc. Rev.* **2014**, *43*, 7746.
- [8] R. D. L. Smith, M. S. Prévot, R. D. Fagan, Z. Zhang, P. A. Sedach, M. K. J. Siu, S. Trudel, C. P. Berlinguette, *Science* **2013**, *340*, 60.
- [9] J. Yang, J. K. Cooper, F. M. Toma, K. A. Walczak, M. Favaro, J. W. Beeman, L. H. Hess, C. Wang, C. Zhu, S. Gul, J. Yano, C. Kisielowski, A. Schwartzberg, I. D. Sharp, *Nat. Mater.* **2017**, *16*, 335.
- [10] M. M. Najafpour, T. Ehrenberg, M. Wiechen, P. Kurz, *Angew. Chem., Int. Ed.* **2010**, *49*, 2233.
- [11] M. M. Thackeray, S. H. Kang, C. S. Johnson, J. T. Vaughey, R. Benedek, S. A. Hackney, *J. Mater. Chem.* **2007**, *17*, 3112.
- [12] V. S. D. Devulapali, M. Richard, T.-Y. Luo, M. L. DeSouza, N. L. Rosi, E. Borguet, *Dalton Trans.* **2021**, *50*, 3116.
- [13] U. Maitra, B. S. Naidu, A. Govindaraj, C. N. R. Rao, *Proc. Natl. Acad. Sci. U. S. A.* **2013**, *110*, 11704.
- [14] C. W. Cady, G. Gardner, Z. O. Maron, M. Retuerto, Y. B. Go, S. Segan, M. Greenblatt, G. C. Dismukes, *ACS Catal.* **2015**, *5*, 3403.
- [15] Z. M. Chan, D. A. Kitchaev, J. N. Weker, C. Schnedermann, K. Lim, G. Ceder, W. Tumas, M. F. Toney, D. G. Nocera, *Proc. Natl. Acad. Sci. U. S. A.* **2018**, *115*, E5261.
- [16] N. Birkner, S. Nayeri, B. Pashaei, M. M. Najafpour, W. H. Casey, A. Navrotsky, *Proc. Natl. Acad. Sci. U. S. A.* **2013**, *110*, 8801.
- [17] P. F. Smith, B. J. Deibert, S. Kaushik, G. Gardner, S. Hwang, H. Wang, J. F. Al-Sharab, E. Garfunkel, L. Fabris, J. Li, G. C. Dismukes, *ACS Catal.* **2016**, *6*, 2089.
- [18] Y. Gorlin, T. F. Jaramillo, *J. Am. Chem. Soc.* **2010**, *132*, 13612.
- [19] D. M. Robinson, Y. B. Go, M. Mui, G. Gardner, Z. Zhang, D. Mastrogiorganni, E. Garfunkel, J. Li, M. Greenblatt, G. C. Dismukes, *J. Am. Chem. Soc.* **2013**, *135*, 3494.
- [20] K. P. Lucht, J. L. Mendoza-Cortes, *J. Phys. Chem. C* **2015**, *119*, 22838.
- [21] S. Levasseur, M. Ménétrier, Y. Shao-Horn, L. Gautier, A. Audemer, G. Demazeau, A. Largeau, C. Delmas, *Chem. Mater.* **2003**, *15*, 348.
- [22] L.-F. Li, Y.-F. Li, Z.-P. Liu, *ACS Catal.* **2020**, *10*, 2581.
- [23] R. C. Remsing, I. G. McKendry, D. R. Strongin, M. L. Klein, M. J. Zdilla, *J. Phys. Chem. Lett.* **2015**, *6*, 4804.
- [24] I. G. McKendry, S. K. Kondaveeti, S. L. Shumlas, D. R. Strongin, M. J. Zdilla, *Dalton Trans.* **2015**, *44*, 12981.
- [25] I. G. McKendry, A. C. Thenuwara, S. L. Shumlas, H. Peng, Y. V. Aulin, P. R. Chinnam, E. Borguet, D. R. Strongin, M. J. Zdilla, *Inorg. Chem.* **2018**, *57*, 557.
- [26] I. G. McKendry, L. J. Mohamad, A. C. Thenuwara, T. Marshall, E. Borguet, D. R. Strongin, M. J. Zdilla, *ACS Energy Lett.* **2018**, *3*, 2280.
- [27] A. C. Thenuwara, S. L. Shumlas, N. H. Attanayake, Y. V. Aulin, I. G. McKendry, Q. Qiao, Y. Zhu, E. Borguet, M. J. Zdilla, D. R. Strongin, *ACS Catal.* **2016**, *6*, 7739.
- [28] A. C. Thenuwara, E. B. Cerkez, S. L. Shumlas, N. H. Attanayake, I. G. McKendry, L. Frazer, E. Borguet, Q. Kang, R. C. Remsing, M. L. Klein, M. J. Zdilla, D. R. Strongin, *Angew. Chem., Int. Ed.* **2016**, *55*, 10381.
- [29] Q. Kang, L. Vernisse, R. C. Remsing, A. C. Thenuwara, S. L. Shumlas, I. G. McKendry, M. L. Klein, E. Borguet, M. J. Zdilla, D. R. Strongin, *J. Am. Chem. Soc.* **2017**, *139*, 1863.
- [30] A. C. Thenuwara, S. L. Shumlas, N. H. Attanayake, E. B. Cerkez, I. G. McKendry, L. Frazer, E. Borguet, Q. Kang, M. J. Zdilla, J. Sun, D. R. Strongin, *Langmuir* **2015**, *31*, 12807.
- [31] H. Peng, I. G. McKendry, R. Ding, A. C. Thenuwara, Q. Kang, S. L. Shumlas, D. R. Strongin, M. J. Zdilla, J. P. Perdew, *Proc. Natl. Acad. Sci. U. S. A.* **2017**, *114*, 9523.
- [32] M. Wiechen, I. Zaharieva, H. Dau, P. Kurz, *Chem. Sci.* **2012**, *3*, 2330.
- [33] H. Yin, H. Li, Y. Wang, M. Ginder-Vogel, G. Qiu, X. Feng, L. Zheng, F. Liu, *Chem. Geol.* **2014**, *381*, 10.
- [34] C. E. Frey, M. Wiechen, P. Kurz, *Dalton Trans.* **2014**, *43*, 4370.
- [35] H. An, Z. Chen, J. Yang, Z. Feng, X. Wang, F. Fan, C. Li, *J. Catal.* **2018**, *367*, 53.
- [36] H. Radinger, P. Connor, R. Stark, W. Jaegermann, B. Kaiser, *ChemCatChem* **2021**, *13*, 1175.
- [37] S. Kosasang, N. Ma, P. Wuamprakhon, N. Phattharasupakun, T. Maihom, J. Limtrakul, M. Sawangphruk, *Chem. Commun.* **2018**, *54*, 8575.
- [38] Wang, Y. O., N. Sakai, K. Fukuda, I. Nakai, Y. Ebina, K. Takada, M. Watanabe, T. Sasaki, *Chem. Mater.* **2003**, *15*, 2873.
- [39] S. H. Kim, S. J. Kim, S. M. Oh, *Chem. Mater.* **1999**, *11*, 557.
- [40] A. Qian, W. Zhang, C. Shi, C. Pan, D. E. Giammar, S. Yuan, H. Zhang, Z. Wang, *Environ. Sci. Technol.* **2019**, *53*, 5768.
- [41] V. Nicolosi, M. Chhowalla, M. G. Kanatzidis, M. S. Strano, J. N. Coleman, *Science* **2013**, *340*, 1226419.
- [42] R. J. Smith, P. J. King, M. Lotya, C. Wirtz, U. Khan, S. De, A. O'Neill, G. S. Duesberg, J. C. Grunlan, G. Moriarty, J. Chen, J. Wang, A. I. Minett, V. Nicolosi, J. N. Coleman, *Adv. Mater.* **2011**, *23*, 3944.
- [43] R. M. McKenzie, *Mineral. Mag.* **1971**, *38*, 493.
- [44] H. W. Nesbitt, G. W. Canning, G. M. Bancroft, *Geochim. Cosmochim. Acta* **1998**, *62*, 2097.
- [45] R. P. Gupta, S. K. Sen, *Phys. Rev. B* **1974**, *10*, 71.
- [46] Y. Zhu, X. Liang, H. Zhao, H. Yin, M. Liu, F. Liu, X. Feng, *Anal. Methods* **2017**, *9*, 103.